

1 **On the radiation belt location in the 23 – 24 solar cycles**

2

3 **Alexei V. Dmitriev^{1,2}**

4 ¹Institute of Space Science, National Central University, Jhongli, Taiwan,

5 ²Skobeltsyn Institute of Nuclear Physics, Lomonosov Moscow State University, Moscow, Russia,

6

7 Corresponding author: Alexei Dmitriev (dalex@jupiter.ss.ncu.edu.tw)

8

9

10 **Abstract**

11 Within the last two solar cycles (from 2001 to 2018), the location of the outer radiation belt (ORB)
12 was determined with using NOAA/Polar-orbiting Operational Environmental Satellite observations
13 of energetic electrons with energies above 30 keV. It was found that the ORB was shifted a little
14 (~1 degrees) in the European and North American sectors while in the Siberian sector, ORB was
15 displaced equatorward by more than 3 degrees. The displacements corresponded qualitatively to
16 the change of geomagnetic field predicted by the IGRF-12 model. However in the Siberian sector,
17 the model has a tendency to underestimate the equatorward shift of ORB. The shift became
18 prominent after 2012 that might be related to a geomagnetic jerk occurred in 2012 – 2013. The
19 displacement of ORB to lower latitudes in the Siberian sector can contribute to an increase in the
20 occurrence rate of mid-latitude auroras observed in the Eastern Hemisphere.

21

22

23

24 **Keywords:** electron radiation belt, secular geomagnetic variation, mid-latitude aurora

25

26 **1. Introduction**

27 The outer radiation belt (ORB) is populated by energetic and relativistic electrons trapped in the
28 magnetosphere at drift shells above $L \sim 3$ (e.g. Ebihara and Miyoshi, 2011). The ORB is very
29 dynamic and exhibits variations in a wide temporal range: short-term storm-time and local time
30 variations, 27-day solar rotation, seasonal and solar cycle variations (e.g. Li et al., 2001; Baker and
31 Kanekal, 2008; Miyoshi and Kataoka, 2011). During magnetic storms, the ORB is substantially
32 disturbed and shifted earthward (Baker et al., 2016; Shen et al., 2017). The storm-time variation is
33 the strongest one for both the ORB location and intensity (Baker and Kanekal, 2008). Magnetic
34 storms produced by interplanetary coronal mass ejecta (ICME) and high-speed streams (HSS) of
35 the solar wind from coronal holes. The seasonal variations with maxima at equinoxes can be
36 explained by the effect of interplanetary magnetic field (IMF) orientation relative to the
37 geomagnetic dipole (Li et al., 2001; O'Brien and McPherron, 2002; McPherron et al., 2009). ORB
38 manifests prominent variations with the solar cycle (Fung et al., 2006; Baker and Kanekal, 2008).
39 It was shown that the maximum of ORB is mostly distant from the Earth in solar minimum
40 (Miyoshi et al., 2004) and it is closest to the Earth during solar maxima (Glauert et al., 2018).
41 Apparently, the intense variations mask relatively weak long-term changes related to a secular
42 variation of the core and crustal magnetic fields. Recently, a number of authors reported significant
43 changes in the Earth's magnetic field. The magnetic axial dipole has decreased over the past 175
44 years by 9% (e.g. Finlay et al., 2016). It was also shown that the north magnetic dip pole, the point
45 where the magnetic field inclination is vertical, drifted from Canada toward Siberia with the speed
46 rapidly increasing from 10 km/yr in 1990s to more than 50 km/yr at present (Chulliat et al., 2010;
47 Thebault et al. 2015). From 1989 to 2002, most dramatic magnetic field changes of >50 nT/yr have
48 been found in the Canadian Arctic and Eastern Siberia.
49 The effects of dipole decay and pole drift are predicted by International Geomagnetic Reference
50 Field 12th generation (IGRF-12) model (e.g. Thebault et al. 2015). However in the Siberian sector,
51 significant anomalies of the main geomagnetic field were found at high latitudes within the 80° - 130°
52 longitudinal range (Gvishiani et al., 2014). In this sense, independent verification of changes in the
53 geomagnetic field at high and middle latitudes is required. Namely, the decrease of magnetic dipole

54 should result in a global equatorward shifting of the magnetospheric domains such as ORB and
55 auroral region. The drift of the north magnetic pole should cause a decrease(increase) of ORB and
56 auroral latitudes in the Siberian(North American) sectors.

57 The long-term changes in the location of auroral region were reported by Smith et al. (2017). They
58 analyzed the latitudinal location of auroral electro jets (AEJs) and revealed a prominent latitudinal
59 displacement of the AEJs by several degrees in the years 2004 – 2014 relative to the previous solar
60 maxima in 1970 and 1980. Namely, in the Siberian sector, AEJ shifted to lower latitudes and in the
61 American sector, AEJ shifted to higher latitudes. The opposite shifts in different sectors cannot be
62 explained by the solar cycle variation and, thus, it has been attributed to the core and crustal
63 magnetic fields. On the other hand, the technique of auroral precipitations is hard to use for tracing
64 of the long-term geomagnetic variations because of high variability in the intensity, location and
65 extension of aurora (e.g. Cresswell-Moorcock et al., 2013; Smith et al.; 2017).

66 An additional support of prominent changes in the geomagnetic field can be found from a sudden
67 increase of occurrence of aurora borealis during the years of 2015 to 2017. There were numerous
68 reports about aurora borealis observed at middle latitudes in the North America, Europe and Russia.
69 Table 1 lists the days when discrete aurora was detected in big Russian cities Moscow (geographic
70 location 55°45N 37°37E), St. Petersburg (geographic location 59°57N 30°18E) and Novosibirsk
71 (geographic location 55°01N 82°55E). It is important to note that while in the North American
72 region, the mid-latitude discrete aurora is observed quite often, this phenomenon is rare at lower
73 magnetic latitudes such as in the regions of Central Europe and in particular in Central Russia
74 (MacDonald et al., 2015; Vázquez et al., 2016). The previous low-latitude aurora borealis was
75 observed during extremely strong geomagnetic storms with minimum $Dst < -300$ nT on October -
76 November 2003 (e.g. Shiokawa et al., 2005; Mikhalev et al., 2004).

77 In contrast, magnetic storms in 2015 – 2017 were not very intense, as one can see in Table 1. The
78 strongest storm on 17 – 18 March 2015, so-called St. Patrick's Day storm, had minimum Dst of
79 -220 nT (e.g. Kataoka et al., 2015). During the St. Patrick's Day storm, aurora borealis was
80 observed worldwide in North America, Central Europe (e.g. "Strongest geomagnetic storm of
81 SC24 sparks spectacular aurora display" at <https://watchers.news/2015/03/18/>) and in a number of

82 cities in Central Russia and Siberia (e.g.
83 <https://www.rt.com/news/241845-aurora-borealis-central-russia/>). Case et al. (2015) found that
84 during the storm, the discrete aurora was observed at unusually low latitudes, which were much
85 lower than those predicted by models of Roble and Ridley (1987) and Newell et al. (2010).
86 The aurora is produced by charged particles precipitating from the magnetosphere to the
87 high-latitude atmosphere. The charged particles move along the magnetic field lines and, thus, the
88 location of precipitation is controlled both by the location of source and by the geomagnetic field
89 configuration. In the present study, we analyze the configuration of the magnetosphere by using
90 observations of energetic electrons from ORB. At low heights, the ORB electrons are observed at
91 middle to high latitudes adjacent to the region of auroral precipitations (Lam et al., 2010). Here we
92 use experimental data on energetic electrons measured by several low-earth orbit (LEO) polar
93 orbiting satellites during the time period from 2001 to 2016. The method of analysis is described in
94 section 2. The results are presented and discussed in sections 3 and 4, respectively. Section 5 is
95 conclusions.

96

97 **2. Method**

98 Energetic electrons in energy ranges >30 keV, >100 keV and >300 keV are measured at LEO by
99 the Medium Energy Proton and Electron Detector (MEPED) instruments on board the
100 NOAA/Polar-orbiting Operational Environmental Satellite (POES) satellites (Evans and Greer,
101 2004; Asikainen and Mursula 2013). Six POES satellites NOAA-16, NOAA-17, NOAA-18,
102 NOAA-19, METOP-01 and METOP-02 (hereafter, P6, P7, P8, P9, P1 and P2, respectively) have
103 Sun-synchronous orbits at altitudes of ~ 800 - 850 km in different local time sectors. Different POES
104 satellites were operating during different years as shown in Table 2.

105 The outer magnetosphere and ORB are very dynamic regions, which are directly controlled by
106 highly variable solar wind plasma streams and interplanetary magnetic field (IMF). As a result, the
107 location of ORB and its high-latitude projection to the heights of LEO vary substantially (e.g.
108 Dmitriev et al., 2010; Rodger et al., 2010). Namely, a strong local time variation is related to the
109 global day-night asymmetry of the magnetosphere such that ORB is observed at higher latitudes

110 during daytime. Variation of geomagnetic tilt angle also causes a change of the ORB latitudinal
111 location. Interplanetary and geomagnetic disturbances result in a prominent equatorward shift of
112 ORB.

113 In order to eliminate the disturbing factors, we consider so-called quiet days. Figure 1
114 demonstrates an example of geomagnetic conditions and measurements of the solar wind plasma
115 and IMF acquired from Wind upstream monitor during quiet day on 23 June 2006. At that day, the
116 solar wind velocity was slow (~ 310 km/s), solar wind dynamic pressure was slightly varying about
117 ~ 1.6 nPa, IMF had northward orientation that resulted in very quiet geomagnetic activity ($AE <$
118 100 nT, $Dst \sim 0$ nT).

119 The list of quiet days selected in the time interval from 2001 to 2018 is presented in Table 2. The
120 solar wind data were acquired from Wind upstream monitor. The selection of quiet days was based
121 on the following criteria:

122 1. The Dst variation was close to 0 and AE index was smaller than 200 nT, i.e. the geomagnetic
123 activity was very weak.

124 2. The solar wind dynamic pressure Pd varied slightly around its average values falling in the
125 range from ~ 1 to 2 nPa.

126 3. The solar wind speed was < 400 km/s and the amplitudes of negative IMF B_z were weak (< 4 nT).

127 Note that the solar wind with the speed of $V > 400$ km/s is often associated with HSSs from
128 coronal holes. Fast solar wind streams initiate the Kelvin-Helmholtz instability at the
129 magnetopause and also produce recurrent magnetic storms, which are accompanied by
130 intensification of wave activity in the outer magnetosphere that results in effective acceleration and
131 radial transport of the ORB electrons (Engebretson et al., 1998; Tsurutani et al., 2006; Horne et al.,
132 2007; Su et al., 2015).

133 4. The quiet days were chosen as long as possible after magnetic storms such that storm-time
134 disturbances of ORB had time to relax. Usually, the quiet days occurred after long-lasting recovery
135 phase of recurrent magnetic storms (Suvorova et al., 2013).

136 The local time variation of ORB latitudinal location was minimized by a choice of narrow LT
137 sector around noon (from 10 to 14 LT). We chose quiet days around June solstice in order to

138 minimize the tilt angle variations. Note that June of 2003 and 2007 was very disturbed and there
139 were no quiet days selected for those years.

140 Figure 2 shows an example of NOAA/POES measurements of energetic electrons in geographic
141 coordinates during the quiet days on 23 June 2006 and 3 June 2016. The geographic maps are
142 composed from data retrieved over multiple orbits of the NOAA/POES satellites in the noon sector
143 (12 ± 2 LT). For each bin of 3° in longitudes and 0.5° in latitudes, we calculate the average flux of
144 electrons measured by the 90° detector of the MEPED instrument. At high latitudes, the detector
145 observes trapped electrons with pitch angles close to 90° , i.e. near the mirror points.

146 The limitation of ORB measurements at given local time is originated from fixed local time of
147 POES satellites at sun synchronous orbits. As one can see in Figure 2 and Table 2, large statistics
148 in the Northern hemisphere can be obtained from a number of POES satellites moving in 2-hour
149 vicinity of local noon around the June solstice. ORB can be easily identified as a wide belt of
150 intense electron fluxes at high latitudes. At middle latitudes, in longitudinal ranges from $\sim 90^\circ\text{E}$ to
151 180°E in the Eastern Hemisphere and from $\sim 80^\circ\text{W}$ to 180°W in the Western Hemisphere, one can
152 also see intense electron fluxes from the inner electron belt and a slot region between the outer and
153 inner belts. The slot region is almost vanished in the maps of subrelativistic electrons with energies
154 >300 keV. Qualitative examination of the ORB location in Figure 2 reveals that in the Eastern
155 Hemisphere, the outer electron belt in 2016 is located few degrees lower in latitudes than that in
156 the year 2006. Most obvious difference can be found for the slot region, which corresponds to the
157 low-latitude boundary of ORB.

158 For quantitative determination of the ORB latitudinal displacement, we analyze electron fluxes in
159 4° vicinities of three longitudes: 80°W (American sector), 0°E (European sector) and 100°E
160 (Siberian sector). Figure 3 shows latitudinal profiles of >30 keV; >100 keV and >300 keV electron
161 fluxes with pitch angles of $\sim 90^\circ$ observed by the NOAA/POES satellites around given longitudes
162 during the quiet days in the years from 2001 to 2018. One can easily identify the maximum of
163 ORB at high latitudes and the slot region at middle latitudes for the American and Siberian sectors.
164 Above the Europe, the slot region is not detected at altitudes of the NOAA/POES orbit.

165 It should be noted that after the year 2014, the experimental data on electrons detected by POES is

166 presented in a different format such that the energy channels of electrons are different from those
167 presented earlier: >40 keV instead of >30 keV, >130 keV instead of >100 keV, and >290 keV
168 instead of >300 keV. Because of that cross-calibration of the electron detectors is difficult. On the
169 other hand, the difference in energies is not very large and, thus, it should not affect strongly the
170 location of ORB. At least the differences are much smaller than the steps between the channels.
171 Therefore, the complex analysis of all three electron channels allows minimization of this effect.

172

173 **3. Results**

174 In Figure 3, the ORB maxima in the American, European and Siberian sectors can be found in the
175 ranges of latitudes from 50° to 58°, from 64° to 70° and from 62° to 74°, respectively. We
176 determine geographic latitude of the maxima for each year with the accuracy of 0.5° to 1°. One can
177 see that the location as well as the intensity of the maximum varies from year to year. The intensity
178 is minimal during the solar minimum in 2009. The fluxes of >300 keV electrons (Figure 3c) were
179 very weak such as determination of the ORB was very difficult. In addition, the ORB maximum
180 above Siberia could not be determined in 2011 because of limited statistics.

181 Qualitatively, the position of ORB maximum above Siberia is more close to 70° and 65°,
182 respectively, in 2001 - 2010 and in 2012 – 2018. Above the Europe and North America, variation
183 of the ORB location is more random. The fluxes of >30 keV electrons in the outer region of ORB
184 are very dynamic because of strong contribution from the auroral population. The latter produced
185 additional maxima at latitudes above 70° and 55°, respectively, in the European-Siberian and
186 American sectors. The additional maxima were very intense in the years 2008, 2010 and 2017 that
187 made difficult to determine the actual location of the ORB. In those cases, we chose the maximum
188 located at lower latitude. This choice gives a good agreement with the ORB maximum location for
189 the >100 keV electrons and especially subrelativistic >300 keV electrons, which are practically
190 free from the auroral contamination.

191 In Figure 3, one can clearly see the slot region between the outer and inner electron belts in the
192 latitudinal ranges 45° - 50° and 45° - 50° above North America and Siberia, respectively. This
193 structure can be well identified and numerically determined, excepting >300 keV electrons. In the

194 case of slot region, the low-latitude edge of ORB is determined as the first high-latitude point of
195 gradual flux enhancement after the slot minimum. Apparently, the electron flux enhancements peak
196 in the maximum of ORB, which location can be determined unambiguously. In the European
197 sector and for the electrons with energies >300 keV, the criterion for determination of the inner
198 edge is not so obvious. It is difficult to define a threshold flux because of strong solar cycle
199 variations of electron fluxes. In this case, the inner edge can be determined as the lowest latitude of
200 gradual decrease of electron fluxes from the ORB maximum toward lower latitudes. As one can
201 see in Figure 3, the inner edge separates usually the background noise with sharply varying fluxes
202 at lower latitudes from smooth and fast increase of ORB fluxes at higher latitudes. Geographic
203 latitude of the inner edge is determined for each year with the accuracy varying from 0.5° to 1° . In
204 the American sector, the inner edge of ORB is situated at lowest latitudes from 43° to 51° , in the
205 European sector – from 55° to 63° , and in the Siberian sector – at highest latitudes from 58° to 65° .
206 In Figure 3, one can find that the latitude of ORB edge above Siberia decreases with years from
207 $\sim 65^\circ$ to 60° for all energy range of electrons. The change of ORB location above the Europe and
208 North America is not so obvious.

209 Figure 4 and Figure 5 show long-term variations in the location of ORB and corresponding
210 predictions of the IGRF-12 model during 17 years from 2001 to 2018. The prediction of IGRF-12
211 model was calculated in the following manner. First, we took a point with given geographic
212 coordinates and calculated its magnetic coordinates for the quiet day on 29 June 2001 using the
213 IGRF model of epoch 2000. Namely, for the ORB maximum, we took points (70°N , 80°W), (66°N ,
214 0°E) and (54°N , 100°E), respectively, for the American, European and Siberian sectors and
215 calculated their geomagnetic coordinates (64.12°N , 11.44°W), (67.05°N , 95.66°E) and (59.5°N ,
216 174.3°E), respectively. For the inner edge of ORB, we took, respectively, (46.5°N , 80°W), (59°N ,
217 0°E) and (63°N , 100°E), with corresponding geomagnetic coordinates (56.62°N , 10.61°W)
218 (60.59°N , 89.34°E) and (52.47°N , 173.7°E). Then we supposed that the geomagnetic coordinates
219 of the points do not change with time and we used them to calculate geographic coordinates from
220 the IGRF-12 model for corresponding quiet days listed in Table 2. The geographic coordinates of a
221 point with given magnetic coordinates should be changed with time because of long-term variation

222 of the geomagnetic field.

223 In Figure 4 and Figure 5, one can see that the ORB maximum and inner edge of >30 keV electrons
224 are usually located at higher latitudes than those of >100 keV electrons, and the ORB of
225 subrelativistic >300 keV electrons is located at lowest latitudes. Note that the location of ORB
226 maximum for >30 keV electrons is scattered significantly and it is different from those for the
227 more energetic electrons because of substantial contamination from the auroral electrons. In
228 contrast, the ORB maxima and inner edge of >100 keV and >300 keV electrons demonstrate very
229 similar dynamics. The location of ORB manifests the well-known solar cycle variation: the
230 latitudes of ORB maximum and inner edge have a tendency to be highest around solar minimum in
231 2008 – 2009 and lowest during solar maxima in the years 2001 and 2012 – 2013. Note that the
232 maximum phases of the 23rd and 24th solar cycles occurred in the years 2000 - 2001 and in 2012 –
233 April 2014, respectively. The years 2008 – 2009 are the solar minimum phase. The declining
234 phases lasted from 2003 to 2007 and from 2014 to 2018. In Figures 4 and 5, one can see that
235 during the declining phase of the current 24th solar cycle (especially in the years 2016 – 2018), the
236 behavior of the ORB maximum and inner edge is different from that during the declining phase of
237 the previous 23rd solar cycle. Namely, their latitudes increased only slightly or even decreased
238 above North America and especially above Siberia.

239 Unfortunately, there is no any model of the ORB location variation with the solar cycle because the
240 driving mechanisms are not well established. On the other hand, the long-term variation in
241 IGRF-12 is almost linear function of the year, as one can see in Figures 4 and 5. Hence, as a first
242 approach for comparative analysis, the variations of ORB location with years are considered as
243 random around a linear function (indicated by dashed strait lines in Figures 4 and 5):

$$244 \quad \lambda = a * \text{year} + b, (1)$$

245 where λ is the latitude of maximum or inner edge of ORB. The slope a , parameter b and their
246 standard errors are calculated from a linear regression for various longitudinal regions and various
247 energies of electrons. The results are presented in Tables 3 and 4 for the ORB maximum and the
248 inner edge, respectively. The linear fits are compared with geomagnetic field trends predicted by
249 the IGRF model. The trends are also fitted by a linear function with the slope a_{IGRF} .

250 In the American sector (see Figure 4a), the latitude of ORB maximum demonstrates a little
251 decrease of about 1° while the IGRF-12 model predicts an increase of $\sim 1^\circ$. The decrease results
252 from relatively low latitudes, where the ORB maximum is located from 2013 to 2018. The location
253 of inner edge of ORB in the American sector (see Figure 5a) does not practically change within the
254 experimental uncertainty of $\sim 1^\circ$. Note that in both cases, the slope a has very large errors (see
255 Tables 3 and 4) such that the slope of IGRF trend $a_{IGRF} = 0.06$ falls almost into the error ranges.
256 Hence, from the statistical consideration one can conclude that the model prediction does not
257 contradict to the observations.

258 In the European sector (Figures 4b and 5b), the IGRF-12 model predicts very small change of 0.3°
259 in the ORB location with the slope $a_{IGRF} \sim 0.02$ that is in good agreement with the ORB maximum
260 dynamics. The location of ORB inner edge for electrons with energies >30 keV and >100 keV
261 demonstrates an increase of $\sim 3^\circ$. However, the slope of increase is determined with a substantial
262 error of up to 50% (see Table 4) that produces an increase by only $\sim 1.5^\circ$. In addition, the >300 keV
263 electrons follow the model and do not exhibit any prominent trend. Hence in the European sector,
264 the IGRF model predicts the ORB dynamics with sufficient accuracy.

265 In the Siberian sector, the IGRF model predicts $\sim 1^\circ$ decrease in the latitude of ORB maximum and
266 inner edge (see Figures 4c and 5c) with the slope $a_{IGRF} \sim -0.06$. From the POES observations, we
267 find that the ORB maximum is displaced to lower latitudes by at least $\sim 3^\circ$ in all electron energy
268 channels: from $\sim 69^\circ$ to $\sim 66^\circ$ for >300 keV electrons, from $\sim 70^\circ$ to 66° for >100 keV electrons and
269 from $\sim 71^\circ$ to 67° for >30 keV electrons (see Figure 4c). The difference is related to very low
270 latitudes ($\sim 67^\circ$ and less) of the ORB maximum during solar maximum and on the declining phase
271 of the current 24th solar cycle in the years 2012 - 2013 and 2016 - 2018, respectively. In the solar
272 maximum and on the declining phase of the previous 23rd solar cycle (the years 2001 and 2004 -
273 2006), the ORB maximum was located at higher latitudes (above 67°). In Table 3, the slopes for all
274 energy ranges are steeper than the slope of IGRF. Note that the errors in determination of the slope
275 a are $\sim 50\%$. Hence statistically, the decrease of latitude might be two times smaller, i.e. $\sim 1.5^\circ$ to 2° .
276 This decrease is slightly larger than 1° of the model prediction, within 0.5° to 1° statistical
277 uncertainty in determination of latitude.

278 Similar pattern can be found for the inner edge of ORB in the Siberian sector (see Figure 5c).
279 Namely, the IGRF model predicts a decrease of $\sim 1^\circ$ with the slope $a_{\text{IGRF}} \sim -0.06$. The inner edge
280 was shifted toward lower latitudes by $\sim 3^\circ$, $\sim 2^\circ$ and $\sim 1^\circ$, respectively, for >30 keV, >100 keV and
281 >300 keV electrons. From Table 4, one can see that the slopes a are steeper than a_{IGRF} . The slopes
282 are calculated with errors of $\sim 30\%$ and $\sim 20\%$, respectively, for >30 keV and >100 keV electrons. It
283 means that the decrease in latitude might be $\sim 2^\circ$ (instead of $\sim 3^\circ$) and $\sim 1.5^\circ$ (instead of $\sim 2^\circ$),
284 respectively. These values are again larger than 1° of the model prediction. Hence, there is a
285 tendency that the change in the latitudinal location of ORB maximum is underestimated by the
286 model. This fact indicates that during 17 years from 2001 to 2018, ORB is abnormally displaced
287 toward the lower latitudes in the Siberian sector.

288 It is interesting to point out the year 2017, when the maximum and inner edge of ORB shifted to
289 very low latitudes of 62° and $\sim 59^\circ$ respectively. The shift was observed during two quiet days on 9
290 and 10 June 2017. Similar pattern of displacement can be found on the declining phase of the
291 previous 23rd solar cycle in the year 2005, when the ORB suddenly shifted equatorward by more
292 than $\sim 2^\circ$. Note that if we exclude the year 2017 from the linear fitting then the results are not
293 practically changed because ORB is located at relatively low latitudes during the years 2012 to
294 2018.

295

296 **4. Discussion**

297 We have found up to 4° equatorward displacement of the ORB in the Siberian sector. The
298 displacement is larger than that predicted by the IGRF-12 model. The difference is statistically
299 significant. It might result both from a change of the geomagnetic field and from changes of
300 driving parameters such as geomagnetic activity, the tilt angle, IMF B_z and solar wind dynamic
301 pressure. It is well known that those parameters affect the latitudinal location of domains in the
302 magnetosphere. The effect of geomagnetic activity was eliminated by the choice of quiet days. The
303 other drivers are considered below.

304 The tilt angle in the noon region at given longitude (80°W , 0°E and 100°E) varies a little ($<2^\circ$)
305 during the June month. The change of local time in 2-hour vicinity of noon produces $\sim 5^\circ$ variation

306 of the tilt angle. The tilt angle variations of a few degrees result in a tiny change of $\sim 0.1^\circ$ in the
307 ORB latitude (e.g. Dmitriev et al., 2010). Hence, we can neglect the effect of tilt angle.

308 The effect of solar wind parameters, including IMF B_z and dynamic pressure (P_d), to the ORB
309 location is not obvious. It is found that the slot region location can be related to the plasmapause
310 but the relation is ambiguous (Darrouzet et al., 2013; Baker et al., 2014). We can make indirect
311 estimation of the effect using a dependence of the cusp location from the solar wind parameters
312 (Kuznetsov et al., 1993; Newell et al., 2006). The equatorward edge of the cusp separates the open
313 and close magnetic field lines in the dayside magnetosphere. Hence the latitude of the equatorward
314 edge can be considered as a proxy of the ORB outer edge. In the first approach, we assume that the
315 effect of solar wind parameters to the ORB location can be represented by the dynamics of the
316 ORB outer edge or the cusp equatorward edge. It can be shown that $B_z = -4$ nT results in less than
317 0.5° equatorward shift of the cusp and a change of P_d from 1 to 2 nPa results in $\sim 0.2^\circ$ decrease in
318 the latitude of the cusp equatorward edge. Hence, the effects of both P_d and IMF B_z are several
319 times weaker than the difference of 3° .

320 Another possible effect is the solar cycle variation. Variations of the ORB location from cycle to
321 cycle and during different phases of solar cycles are still poorly investigated. It was well
322 established that during solar minima and maxima, the ORB is located, respectively, at highest and
323 lowest latitudes (Miyoshi et al., 2004; Glauert et al., 2018). From these findings, we can speculate
324 that lower(higher) solar activity results in an increase (a decrease) of the ORB latitudes. In Figure
325 3, one can see that the intensities of electrons are weaker after the beginning of the 24th solar
326 maximum in 2012 in comparison with the 23rd solar cycle. Note that the 23rd solar cycle was
327 stronger than the 24th one. Following this logic, the ORB should be located at relatively higher
328 latitudes during the weak 24th solar cycle than during the strong 23rd solar cycle.

329 In Figure 6, the outer radiation belt location is compared during the maximum and declining
330 phases of the solar cycles 23rd (the years 2001 – 2006) and 24th (the years 2013 – 2018). During
331 those time intervals, the sunspot numbers for the both cycles correlate very well. The ORB
332 location demonstrates also very similar solar cycle variations. The ORB latitude increased after the
333 solar maximum in 2001 – 2002 (and in corresponding years 2013 – 2014). During those years, the

334 ORB location was quite close for the both cycles. The difference of $\sim 1^\circ$ can be explained by the
335 secular variation predicted by the IGRF model. During the declining phase in 2004 – 2005 (2015 –
336 2017), the ORB was shifted to lower latitudes and then it moved slightly poleward in 2006 (2018),
337 when the solar minimum was approached.

338 From Figure 6, one can clearly see that on the declining phase of the 24th solar cycle, the outer
339 radiation belt is located at latitudes lower by several degrees than those during the 23rd solar cycle.
340 It is interesting to point out the year 2017, when the maximum and inner edge of ORB were shifted
341 to very low latitudes of 62° and $\sim 59^\circ$ respectively. The shift was observed during two quiet days on
342 9 and 10 June 2017. Similar pattern of strong displacement by more than $\sim 2^\circ$ can be found on the
343 declining phase of the previous 23rd solar cycle in 2005, the year corresponding to the similar
344 stage of solar activity. Hence, the ORB dynamics in the year of 2017, as well as during the whole
345 declining phase from 2014 to 2018, was not anomalous in the sense of solar cycle variations.
346 However, the ORB latitudes were abnormally low. The difference of several degrees cannot be
347 explained by the IGRF model. As a result, we have found totally opposite effect: ORB over Siberia
348 is located at lower latitudes during the weak 24th solar cycle than during the strong 23rd solar
349 cycle. It should be noted that if one excludes the year 2017 from the linear fitting then the results
350 are not practically changed because ORB is located at relatively low latitudes during practically
351 whole declining phase of the 24th solar cycle.

352 From the above, we can conclude that the difference between the observations and predictions can
353 be rather originated from anomalous dynamics of the geomagnetic field. This idea is supported by
354 the observations of ORB location over the Europe and North America, where the ORB
355 displacement is well predicted by the IGRF-12 model. An additional support can be found from
356 results of long-term magnetic observations in Siberia where significant anomalies of the main
357 geomagnetic field have been revealed in the 80° - 130° longitudinal range (Gvishiani et al., 2014).
358 Namely, the IGRF-12 model predicted the magnetic field up to 300 nT stronger than that measured
359 by ground based magnetic stations that was close to 0.5% of the total magnetic field in this region.
360 For the geodipole, stronger magnetic field corresponds to higher latitudes.

361 In Figures 4c and 5c, one can see that the decrease of ORB latitude in the Siberian sector is most

362 prominent after 2012. On the other hand in the years 2012 –2013, a sudden change was found in
363 the acceleration of secular variation in the geomagnetic field (Finlay et al., 2015). Analyzing time
364 interval from 1999 to 2015, Finlay et al. (2015) revealed 3 pulses in time evolution of the mean
365 square secular acceleration power: in 2006, in 2009 and in 2012 – 2013. Chulliat et al. (2015)
366 attribute these pulses, or so-called sharp geomagnetic "jerks", to magnetic field variations
367 originating in the Earth's core. We can assume that the abnormal ORB displacement might be
368 related to the geomagnetic jerks. We can assume that the abnormal ORB displacement might be
369 related to the geomagnetic jerks. Though, there is no prominent change in the ORB location in 2006, one
370 can indicate very high latitude of ORB in 2009. Note that the jerk in 2009 coincided with the abnormally
371 deep solar minimum and, hence, it could be hard to distinguish between the two effects. On the other hand,
372 we have found significant change in the ORB dynamics after 2012 – 2013.

373 The several degrees equatorward displacement of ORB in the Siberian sector indicates an
374 equatorward shifting of all domains in the magnetosphere, including the region of auroral
375 precipitations. Apparently, the shifting contributes to the increase in occurrence rate of the
376 mid-latitude auroras in Siberia and, perhaps, in entire Russia. In addition, Finlay et al. (2015)
377 expect that the next jerk might occur around 2016. We do not have any reports about the recent
378 jerks yet. But very strong decrease of the ORB latitude observed in 2017 might indicate the sudden
379 change in the geomagnetic field.

380

381 **5. Conclusions**

382 NOAA/POES observations of electrons with energies of few tens and hundreds of keV allowed
383 revealing and measure a latitudinal displacement of the outer radiation belt during last 18 years.
384 The displacement corresponds qualitatively to the change of geomagnetic field predicted by the
385 IGRF-12 model. However in the Siberian sector, the model has a tendency to underestimate the
386 equatorward shift of ORB. The shift became prominent after 2012 that might be related to the
387 geomagnetic jerk occurred in 2012 – 2013. The increase in the occurrence rate of mid-latitude
388 auroras in the Eastern Hemisphere can be explained, at least partially, by the equatorward
389 displacement of the high-latitude projection of the magnetosphere domains.

390
391 **Acknowledgments** The authors thank a team of NOAA's Polar Orbiting Environmental Satellites
392 for providing experimental data about energetic particles, the CDAWEB for providing the Wind
393 solar wind data, Kyoto World Data Center for Geomagnetism
394 (<http://wdc.kugi.kyoto-u.ac.jp/igrf/point/index.html>) for providing the geomagnetic indices and
395 computation of the IGRF12 model, and WDC-SILSO, Royal Observatory of Belgium, Brussels for
396 providing sunspot numbers (<http://www.sidc.be/silso/datafiles>). The work was supported by grant
397 MOST-106-2111-M-008-015-, R&D foundation from National Central University and partially by
398 grant NSC103-2923-M-006-002-MY3/14-05-92002HHC_a of Taiwan - Russia Research
399 Cooperation.
400

401 **References**

- 402 Asikainen, T., and Mursula, K.: Correcting the NOAA/MEPED energetic electron fluxes for
403 detector efficiency and proton contamination, *J. Geophys. Res. Space Physics*, 118,
404 doi:10.1002/jgra.50584, 2013.
- 405 Baker, D. N., and Kanekal, S. G.: Solar cycle changes, geomagnetic variations, and energetic
406 particle properties in the inner magnetosphere, *Journal of Atmospheric and Solar-Terrestrial*
407 *Physics*, 70, 195–206, doi: 10.1016/j.jastp.2007.08.031, 2008.
- 408 Baker, D. N. et al.: An impenetrable barrier to ultrarelativistic electrons in the Van Allen radiation
409 belts, *Nature*, 515, 531 - 534, doi: 10.1038/nature13956, 2014.
- 410 Baker, D. N., Jaynes, A. N., Kanekal, S. G., Foster, J. C., Erickson, P. J., Fennell, J. F., Blake, J. B.,
411 Zhao, H., Li, X., Elkington, S. R., Henderson, M. G., Reeves, G. D., Spence, H. E., Kletzing, C.
412 A., and Wygant, J. R.: Highly relativistic radiation belt electron acceleration, transport, and loss:
413 Large solar storm events of March and June 2015, *J. Geophys. Res. Space Physics*, 121,
414 6647-6660, doi:10.1002/2016JA022502, 2016.
- 415 Case, N. A., MacDonald, E. A., and Patel, K. G.: Aurorasaurus and the St Patrick's Day storm,
416 *Astronomy & Geophysics* 56(3), 13-14. DOI: 10.1093/astrogeo/atv089, 2015.
- 417 Chulliat, A., Hulot, G., and Newitt, L. R.: Magnetic flux expulsion from the core as a possible
418 cause of the unusually large acceleration of the north magnetic pole during the 1990s, *J.*
419 *Geophys. Res.*, 115, B07101, doi:10.1029/2009JB007143, 2010.
- 420 Chulliat A., Alken, P., and Maus, S.: Fast equatorial waves propagating at the top of the Earth's
421 core. *Geophys Res Lett.*, 42(9), 3321-3329, doi:10.1002/2015GL064067, 2015.

422 Cresswell-Moorcock, K., Rodger, C. J., Kero, A., Collier, A. B., Clilverd, M. A., Häggström, I.,
423 and Pitkänen, T.: A reexamination of latitudinal limits of substorm-produced energetic electron
424 precipitation, *J. Geophys. Res. Space Physics*, 118, 6694-6705, doi:10.1002/jgra.50598, 2013.

425 Darrouzet, F., Pierrard, V., Benck, S., Lointier, G., Cabrera, J., Borremans, K., Ganushkina, N. Yu.,
426 and Keyser, J. De.: Links between the plasmopause and the radiation belt boundaries as
427 observed by the instruments CIS, RAPID and WHISPER onboard Cluster, *J. Geophys. Res.*
428 *Space Physics*, 118, 4176-4188, doi:10.1002/jgra.50239, 2013.

429 Dmitriev, A. V., Jayachandran, P. T., and Tsai, L.-C.: Elliptical model of cutoff boundaries for the
430 solar energetic particles measured by POES satellites in December 2006, *J. Geophys. Res.*, 115,
431 A12244, doi:10.1029/2010JA015380, 2010.

432 Ebihara Y., and Y. Miyoshi (2011): Dynamic inner magnetosphere: A tutorial and recent advances,
433 in Liu W., Fujimoto M. (eds) *The dynamic magnetosphere*, 145 – 187, doi:
434 10.1007/978-94-007-0501-2_9

435 Engebretson, M., Glassmeier, K.-H., Stellmacher, M., Hughes, W. J., and Luhr, H.: The
436 dependence of high-latitude Pc5 wave power on solar wind velocity and on the phase of
437 high-speed solar wind streams, *J. Geophys. Res.*, 103, 26,271-26,283, doi:10.1029/97JA03143,
438 1998.

439 Evans, D. S., and Greer, M. S.: *Polar Orbiting Environmental Satellite Space Environment Monitor:*
440 *2. Instrument Descriptions and Archive Data Documentation*, Tech. Memo. Version 1.4, NOAA
441 Space Environ. Lab., Boulder, Colo., 2004.

442 Fung, S. F., Shao, X. and Tan L. C.: Long-term variations of the electron slot region and global

443 radiation belt structure, *Geophys. Res. Lett.*, 33, L04105, doi:10.1029/2005GL024891, 2006.

444 Finlay, C. C., Aubert, J., and Gillet, N.: Gyre-driven decay of the Earth's magnetic dipole, *Nat.*
445 *Commun*, 7:10422, 1 - 8, doi: 10.1038/ncomms10422, 2016.

446 Glauert, S. A., Horne, R. B., and Meredith, N. P.: A 30-year simulation of the outer electron
447 radiation belt, *Space Weather*, 16, 1498-1522. <https://doi.org/10.1029/2018SW001981>, 2018.

448 Gvishiani, A., Lukianova, R., Soloviev, A., Khokhlov, A.: Survey of Geomagnetic Observations
449 Made in the Northern Sector of Russia and New Methods for Analysing Them, *Surv.*
450 *Geophys.*,35, 1123-1154, DOI 10.1007/s10712-014-9297-8, 2014.

451 Horne, R. B., Thorne, R. M., Glauert, S. A., Meredith, N. P., Pokhotelov, D., and Santolik, O.:
452 Electron acceleration in the Van Allen radiation belts by fast magnetosonic waves, *Geophys.*
453 *Res. Lett.*, 34, L17107, doi:10.1029/2007GL030267, 2007.

454 Kataoka, R., Shiota, D., Kilpua, E., and Keika, K.: Pileup accident hypothesis of magnetic storm
455 on 17 March 2015, *Geophys. Res. Lett.*, 42, 5155-5161, doi:10.1002/2015GL064816, 2015.

456 Kuznetsov, S.N., Suvorova, A.V., and Tolstaya, E.D.: Relationship of the cleft latitude to
457 interplanetary parameters and DST variations, *Cosmic Research*, 31(4), 409-415 (Translated
458 from *Kosmicheskie Issledovaniya*), 1993.

459 Lam, M. M., Horne, R. B., Meredith, N. P., Glauert, S. A., Moffat-Griffin, T., and Green, J. C.:
460 Origin of energetic electron precipitation >30 keV into the atmosphere, *J. Geophys. Res.*, 115,
461 A00F08, doi:10.1029/2009JA014619, 2010.

462 Li, X., Baker, D. N., Kanekal, S. G., Looper, M., and Temerin, M.: Long term measurements of
463 radiation belts by SAMPEX and their variations, *Geophys. Res. Lett.*, 28(20), 3827-3830, DOI:

464 10.1029/2001GL013586, 2001.

465 MacDonald, E. A., Case, N. A., Clayton, J. H., Hall, M. K., Heavner, M., Lalone, N., Patel, K. G.,
466 and Tapia, A.: Aurorasaurus: A citizen science platform for viewing and reporting the aurora,
467 *Space Weather*, 13, doi:10.1002/2015SW001214, 2015.

468 McPherron, Baker, D. N., and Crooker, N. U.: Role of the Russell-McPherron effect in the
469 acceleration of relativistic electrons, *Journal of Atmospheric and Solar-Terrestrial Physics*, 71,
470 1032-1044, doi: 10.1016/j.jastp.2008.11.002, 2009.

471 Mikhalev, A. V., Beletsky, A. B., Kostyleva, N. V., and Chernigovskaya, M. A.: Midlatitude
472 Auroras in the South of Eastern Siberia during Strong Geomagnetic Storms on October 29-31,
473 2003 and November 20-21, 2003, *Cosmic Research*, 42(6), 591-596 (Translated from
474 *Kosmicheskie Issledovaniya*, 42(6), 616-621), 2004.

475 Miyoshi, Y. and Kataoka, R.: Solar cycle variations of outer radiation belt and its relationship to
476 solar wind structure dependences, *Journal of Atmospheric and Solar-Terrestrial Physics*, 73(10),
477 77-87, doi:10.1016/j.jastp.2010.09.031, 2011.

478 Miyoshi, Y. S., Jordanova, V. K., Morioka, A., and Evans, D. S.: Solar cycle variations of the
479 electron radiation belts: Observations and radial diffusion simulation, *Space Weather*, 2,
480 S10S02, doi:10.1029/2004SW000070, 2004.

481 Newell, P. T., Sotirelis, T., Liou, K., Meng, C.-I., and Rich, F. J.: Cusp latitude and the optimal
482 solar wind coupling function, *J. Geophys. Res.*, 111, A09207, doi:10.1029/2006JA011731,
483 2006.

484 Newell, P. T., Sotirelis, T., and Wing, S.: Seasonal variations in diffuse, monoenergetic, and

485 broadband aurora, *J. Geophys. Res.*, 115, A03216, doi:10.1029/2009JA014805, 2010.

486 O'Brien, T. P., and McPherron, R. L.: Seasonal and diurnal variation of Dst dynamics, *J. Geophys.*
487 *Res.*, 107(A11), 1341, doi:10.1029/2002JA009435, 2002.

488 Roble, R. G., and Ridley, E. C.: An auroral model for the NCAR thermospheric general circulation
489 model (TGCM), *Ann. Geophys.*, 5, 369-382, 1987.

490 Rodger, C. J., Clilverd, M. A., Green, J. C., and Lam, M. M.: Use of POES SEM-2 observations to
491 examine radiation belt dynamics and energetic electron precipitation into the atmosphere, *J.*
492 *Geophys. Res.*, 115, A04202, doi:10.1029/2008JA014023, 2010.

493 Shen, X.-C., Hudson, M. K., Jaynes, A., Shi, Q., Tian, A., Claudepierre, S., Qin, M.-R., Zong, Q.-G.,
494 and Sun, W.-J.: Statistical study of the storm time radiation belt evolution during Van Allen
495 Probes era: CME- versus CIR-driven storms, *J. Geophys. Res. Space Physics*, 122, 8327-8339,
496 doi:10.1002/2017JA024100, 2017.

497 Shiokawa, K., Ogawa, T., and Kamide, Y.: Low-latitude auroras observed in Japan: 1999–2004, *J.*
498 *Geophys. Res.*, 110, A05202, doi:10.1029/2004JA010706, 2005.

499 Smith, A. R. A., Beggan, C. D., Macmillan, S., and Whaler, K. A.: Climatology of the auroral
500 electrojets derived from the along-track gradient of magnetic field intensity measured by
501 POGO, Magsat, CHAMP, and Swarm. *Space Weather*, 15,
502 <https://doi.org/10.1002/2017SW001675>, 2017.

503 Su, Z. et al.: Ultra-low-frequency wave-driven diffusion of radiation belt relativistic electrons, *Nat.*
504 *Commun.*, 6:10096, doi: 10.1038/ncomms10096, 2015.

505 Suvorova, A. V., Dmitriev, A. V., Tsai, L.-C., Kunitsyn, V. E., Andreeva, E. S., Nesterov, I. A., and

506 Lazutin, L. L.: TEC evidence for near-equatorial energy deposition by 30 keV electrons in the
507 topside ionosphere, *J. Geophys. Res. Space Physics*, 118, 4672-4695, doi:10.1002/jgra.50439,
508 2013.

509 Thebault E. et al.: International Geomagnetic Reference Field: the 12th generation, *Earth, Planets*
510 *and Space*, 67:79, 2 – 19, doi 10.1186/s40623-015-0228-9, 2015.

511 Tsurutani, B. T., et al.: Corotating solar wind streams and recurrent geomagnetic activity: A review,
512 *J. Geophys. Res.*, 111, A07S01, doi:10.1029/2005JA011273, 2006.

513 Vázquez, M., Vaquero, J. M., Gallego, M. C., Roca Cortés, T., Pallé, P. L.: Long-Term Trends and
514 Gleissberg Cycles in Aurora Borealis Records (1600 - 2015), *Solar Phys* 291, 613-642, DOI
515 10.1007/s11207-016-0849-6, 2016.

516

517 **Table 1.** Observations of discrete aurora in Russia in the years 2015 to 2016

| Date | min Dst, nT | City | Geomagnetic location | Reference |
|---------------------|----------------|----------------|-------------------------|-----------|
| 2015 March 17-18 | -220 | Moscow | 51°16N 122°06E | Ref1 |
| 2015 June 22-23 | -200 | Moscow | 51°16N 122°06E | Ref2 |
| 2015 August 16-17 | -84 | St. Petersburg | 56°23N 117°36E | Ref3 |
| 2015 October 7-8 | -120 | St. Petersburg | 56°23N 117°36E | Ref4 |
| 2016 February 17-18 | -50 | St. Petersburg | 56°24N 117°37E | Ref5 |
| 2016 April 3-4 | -50 | St. Petersburg | 56°24N 117°37E | Ref6 |
| 2016 August 24-25 | -80 | St. Petersburg | 56°24N 117°37E | Ref7 |
| 2017 September 7-8 | -124 | Novosibirsk | 45°56N 160°07E | Ref8 |
| 2017 November 7-8 | -74 | St. Petersburg | 56°25N 117°38E | Ref9 |

518 Ref1 - www.dp.ru/a/2015/03/18/Severnoe_sijanie_uvideli_zh/

519 Ref2 - www.dp.ru/a/2015/06/23/Severnoe_sijanie_uvideli_v/

520 Ref3 - <http://47news.ru/articles/92419/>

521 Ref4 - www.dp.ru/a/2015/10/08/Severnoe_sijanie_v_Peterbu/

522 Ref5 - www.fontanka.ru/2016/02/17/058/

523 Ref6 - www.dp.ru/a/2016/04/03/ZHiteli_Peterburga_deljatsja/

524 Ref7 - www.fontanka.ru/2016/08/24/035/ and www.topnews.ru/news_id_92986.html

525 Ref8 - <http://www.ntv.ru/video/1515160/>

526 Ref9 - <https://www.fontanka.ru/2017/11/07/134/>

527

529 **Table 2.** List of quiet days in June selected for POES observations of the outer radiation belt.

| Year | Day in June | Start UT | Duration, hours | V* km/s | Pd** nPa | Bz _{min} [§] nT | POES Satellites [#] |
|------|-------------|----------|-----------------|---------|-----------------|-----------------------------------|------------------------------|
| 2001 | 29 | 0 | 24 | 350 | 1.6 (1.0 – 3.2) | 0.6 (-4) | P6 |
| 2002 | 28 | 0 | 24 | 340 | 1.2 (0.8 – 1.8) | 2.2 (-3) | P6 |
| 2004 | 24 | 12 | 24 | 330 | 1.1 (0.5 – 2.5) | 1.2 (-2) | P6, P7 |
| 2005 | 21 | 0 | 18 | 350 | 0.9 (0.5 – 2.0) | 3.1 (-4) | P6, P7, P8 |
| 2006 | 23 | 0 | 24 | 310 | 1.6 (1.1 – 2.3) | 3.4 (-1) | P6, P7, P8 |
| 2008 | 13 | 0 | 24 | 310 | 1.5 (0.8 – 1.9) | 1.8 (-0.8) | P2, P7, P8 |
| 2009 | 17 | 0 | 24 | 300 | 1.1 (0.5 – 1.7) | 1.9 (-3) | P2, P7, P8, P9 |
| 2010 | 12 | 0 | 24 | 350 | 1.1 (0.6 – 2.4) | 0.2 (-2) | P2, P7, P8, P9 |
| 2011 | 28 | 6 | 24 | 390 | 0.8 (0.5 – 1.7) | 1.8 (-2) | P2, P6, P8, P9 |
| 2012 | 15 | 0 | 24 | 320 | 0.8 (0.5 – 1.3) | 0.0 (-3) | P2, P6, P8, P9 |
| 2013 | 16 | 0 | 24 | 330 | 0.9 (0.6 - 1.5) | 1.0 (-3) | P2, P6, P8, P9 |
| 2014 | 1 | 0 | 36 | 300 | 1.7 (1.1 – 4.0) | 1.5 (-4) | P1, P2, P9 |
| 2015 | 4 | 0 | 24 | 280 | 1.0 (0.7 – 1.7) | 0.9 (-3) | P1, P2, P9 |
| 2016 | 3 | 0 | 24 | 300 | 1.0 (0.7 – 1.4) | -0.3 (-3) | P1, P2, P9 |
| 2017 | 9 | 6 | 24 | 310 | 1.9 (1.0 – 2.6) | -1.3 (-4) | P1, P2, P9 |
| 2018 | 12 | 8 | 24 | 300 | 1.3 (0.9 – 2.0) | 0.0 (-4) | P1, P2, P9 |

530 *Daily average of the solar wind velocity

531 **Daily average of the solar wind dynamic pressure and its minimum and maximum in brackets

532 [§]Daily average Bz component of the interplanetary magnetic field and Bz minimum in brackets

533 #POES satellites observed the outer radiation belt

534

535 **Table 3.** Coefficients of the best linear fit of the latitudinal change of the ORB maximum location
 536 with years for various longitudes and energy of electrons

| Longitude, deg | Energy, keV | a_{IGRF} , deg/year | a , deg/year |
|----------------|-------------|------------------------------|--------------------|
| -80 | >30 | 0.06 ± 0.003 | -0.153 ± 0.112 |
| -80 | >100 | 0.06 ± 0.003 | -0.069 ± 0.097 |
| -80 | >300 | 0.06 ± 0.003 | -0.057 ± 0.084 |
| 0 | >30 | 0.018 ± 0.001 | 0.021 ± 0.089 |
| 0 | >100 | 0.018 ± 0.001 | -0.032 ± 0.063 |
| 0 | >300 | 0.018 ± 0.001 | -0.027 ± 0.042 |
| 100 | >30 | -0.06 ± 0.003 | -0.265 ± 0.119 |
| 100 | >100 | -0.06 ± 0.003 | -0.208 ± 0.106 |
| 100 | >300 | -0.06 ± 0.003 | -0.167 ± 0.084 |

537
 538
 539 **Table 4.** Coefficients of the best linear fit of the latitudinal change of the ORB inner edge location
 540 with years for various longitudes and energy of electrons.

| Longitude, deg | Energy, keV | a_{IGRF} , deg/year | a , deg/year |
|----------------|-------------|------------------------------|--------------------|
| -80 | >30 | 0.06 ± 0.003 | -0.029 ± 0.065 |
| -80 | >100 | 0.06 ± 0.003 | -0.021 ± 0.059 |
| -80 | >300 | 0.06 ± 0.003 | -0.014 ± 0.063 |
| 0 | >30 | 0.019 ± 0.001 | 0.195 ± 0.107 |
| 0 | >100 | 0.019 ± 0.001 | 0.241 ± 0.078 |
| 0 | >300 | 0.019 ± 0.001 | 0.032 ± 0.069 |
| 100 | >30 | -0.06 ± 0.003 | -0.183 ± 0.058 |
| 100 | >100 | -0.06 ± 0.003 | -0.211 ± 0.037 |
| 100 | >300 | -0.06 ± 0.003 | -0.097 ± 0.069 |

541
 542

543 **Figure captions**

544
545 Figure 1. Solar wind and geomagnetic conditions on 22 to 24 June 2006 (from top to bottom):
546 solar wind bulk velocity V ; solar wind dynamic pressure P_d ; interplanetary magnetic field
547 magnitude B (blue dotted curve) and B_z component (black solid curve); auroral electrojet index
548 AE ; storm-time Dst index. The day on 23 June (indicated by vertical red dashed lines) is very quite
549 in the solar wind and geomagnetic parameters.

550
551 Figure 2. Geographic maps of energetic electron fluxes with energies >300 keV (a,b), >100 keV
552 (c,d), >30 keV (e,f) and pitch angles of $\sim 90^\circ$ observed by POES satellites at height of ~ 850 km in 2
553 hour vicinity of local noon (left column) on 23 June 2006 and (right column) on 2 June 2016. The
554 solid wide curve indicates the geomagnetic equator. The outer and inner electron belts and a slot
555 region between them are clearly seen (excepting of >300 keV electrons), respectively, at high and
556 middle latitudes in the longitudinal range from $\sim 90^\circ$ E to $\sim 80^\circ$ W.

557
558 Figure 3. Latitudinal profiles of electron fluxes with pitch angles of $\sim 90^\circ$ observed by POES
559 satellites during quiet days in different years at height of ~ 850 km in vicinity of local noon at
560 longitudes around 100° E (red circles), 0° E (blue crosses), and 80° W (black diamonds) for various
561 energy channels: (a) >30 keV, (b) >100 keV, and (c) >300 keV. Vertical dashed and solid lines
562 indicate latitudes of the maximum and inner edge of the outer radiation belt, respectively.

563
564 Figure 4. Geographic latitude of the maximum of the outer radiation belt measured at height of
565 ~ 850 km during geomagnetic quiet days around 80° W (a), 0° E (b), and 100° E (c) for electrons
566 with energies of >30 keV (red circles), >100 keV (blue crosses), and >300 keV (green triangles).
567 Dashed curves of corresponding colors show the best linear fit of the latitudinal change of the
568 maximum location with years (see Table 3). Solid black curves show the latitudinal change
569 predicted by the IGRF model of corresponding epochs (see details in the text). The grey curve
570 shows sunspot number (right axis).

571
572 Figure 5. The same as Figure 4 but for the inner edge of the outer radiation belt. Coefficients of the
573 best linear fit are presented in Table 4.
574
575 Figure 6. Geographic latitude of the inner edge (a) and maximum (b) of the outer radiation belt
576 measured during geomagnetic quiet days at height of ~850 km around longitude of 100°E for
577 electrons with energies of >30 keV (circles), >100 keV (crosses), and >300 keV (triangles).
578 Bottom panels show the sunspot number in the 23rd solar cycle (the years 2001 – 2006, black
579 curves) and in the 24th solar cycle (the years 2013 – 2018, blue curves). The outer radiation belt
580 location is shown by black and red symbols, respectively, for the 23rd and 24th solar cycles. It can
581 be seen that on the declining phase of the 24th solar cycle, the outer radiation belt is systematically
582 located at lower latitudes than that during the 23rd solar cycle.
583

584
585
586
587
588
589
590
591
592
593
594
595
596
597
598
599
600
601
602
603
604
605

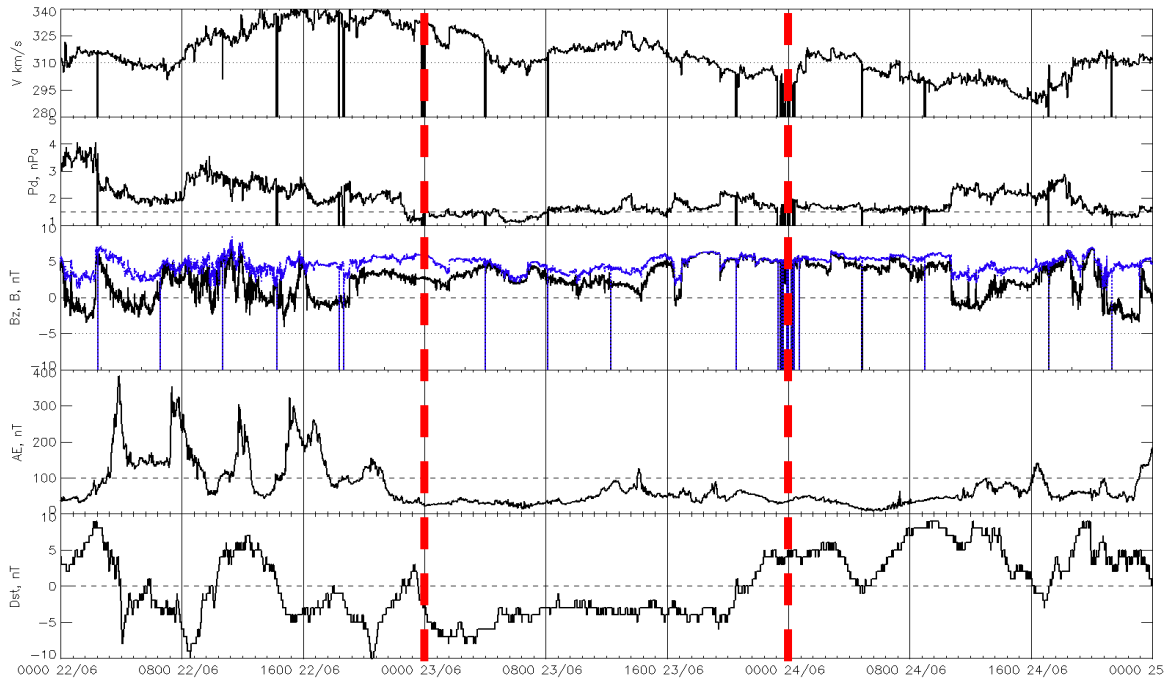
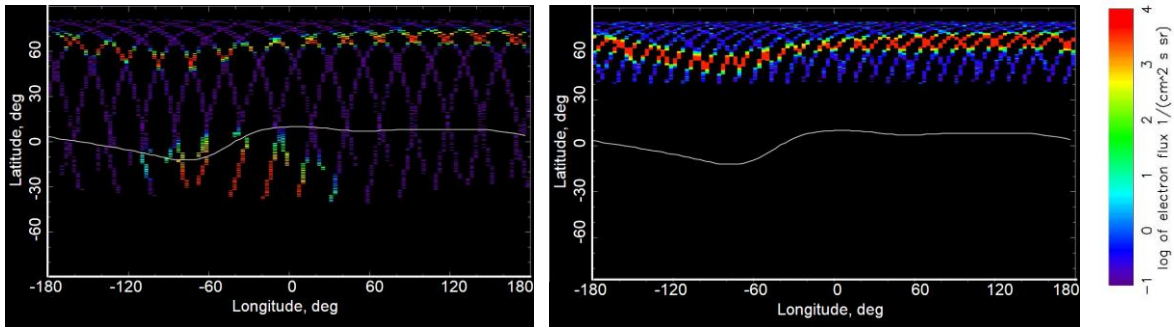


Figure 1. Solar wind and geomagnetic conditions on 22 to 24 June 2006 (from top to bottom): solar wind bulk velocity V ; solar wind dynamic pressure P_d ; interplanetary magnetic field magnitude B (blue dotted curve) and B_z component (black solid curve); auroral electrojet index AE ; storm-time Dst index. The day on 23 June (indicated by vertical red dashed lines) is very quite in the solar wind and geomagnetic parameters.

606
607

2006

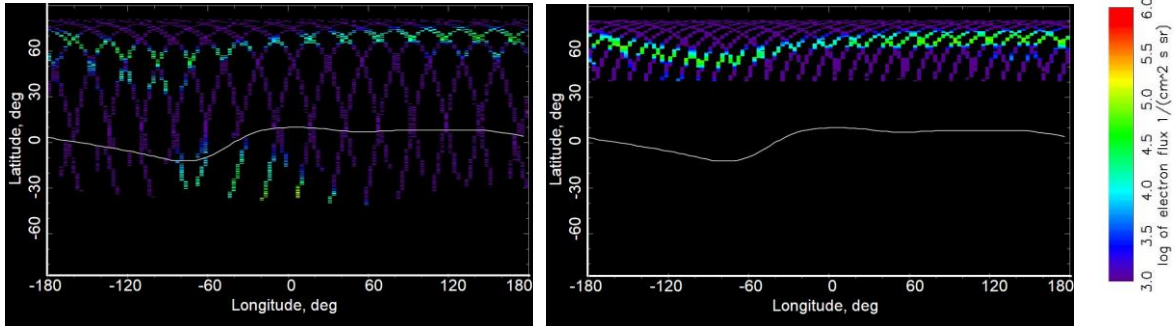
2016



608
609

a

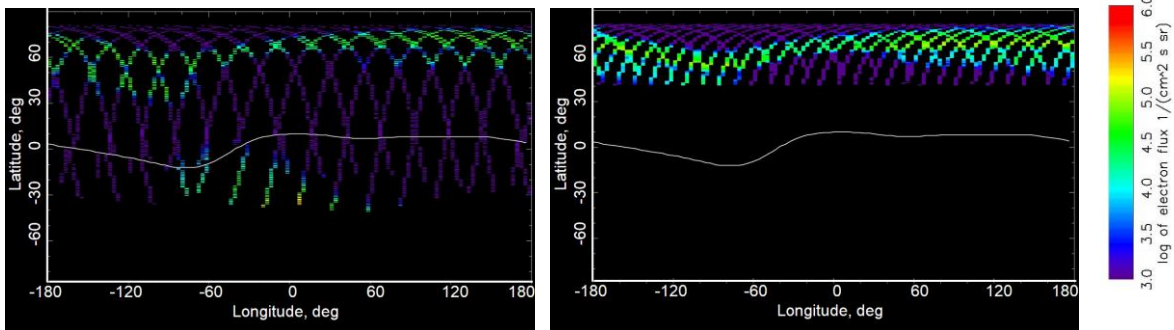
b



610
611

c

d



612
613

e

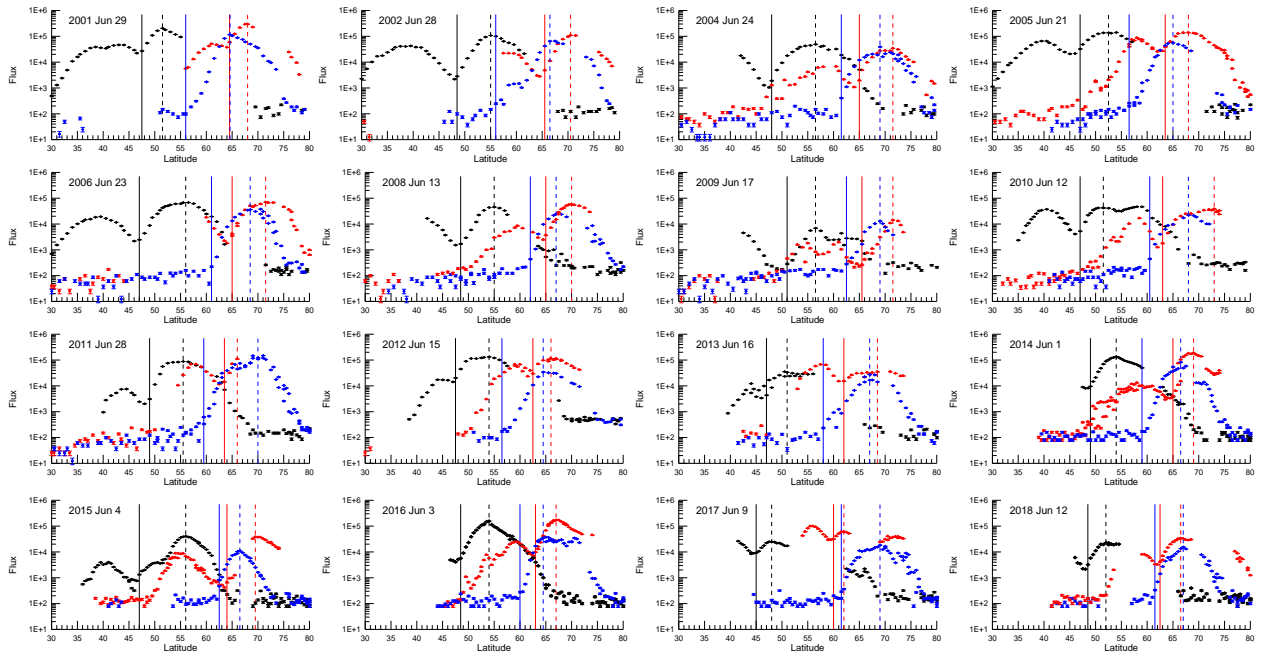
f

614

615 Figure 2. Geographic maps of energetic electron fluxes with energies >300 keV (a,b), >100 keV
616 (c,d), >30 keV (e,f) and pitch angles of $\sim 90^\circ$ observed by POES satellites at height of ~ 850 km in 2
617 hour vicinity of local noon (left column) on 23 June 2006 and (right column) on 3 June 2016. The
618 solid wide curve indicates the geomagnetic equator. The outer and inner electron belts and a slot
619 region between them are clearly seen (excepting of >100 keV electrons), respectively, at high and
620 middle latitudes in the longitudinal range from $\sim 90^\circ$ E to $\sim 80^\circ$ W.

621

622

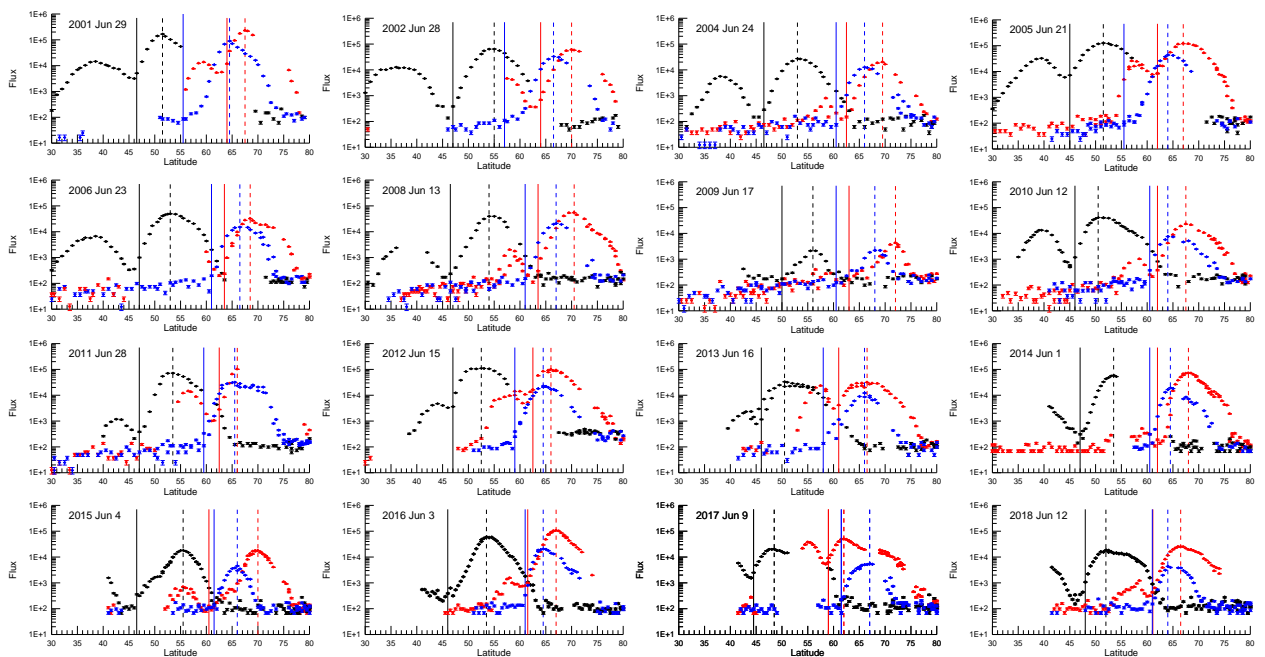


623

624

625

a

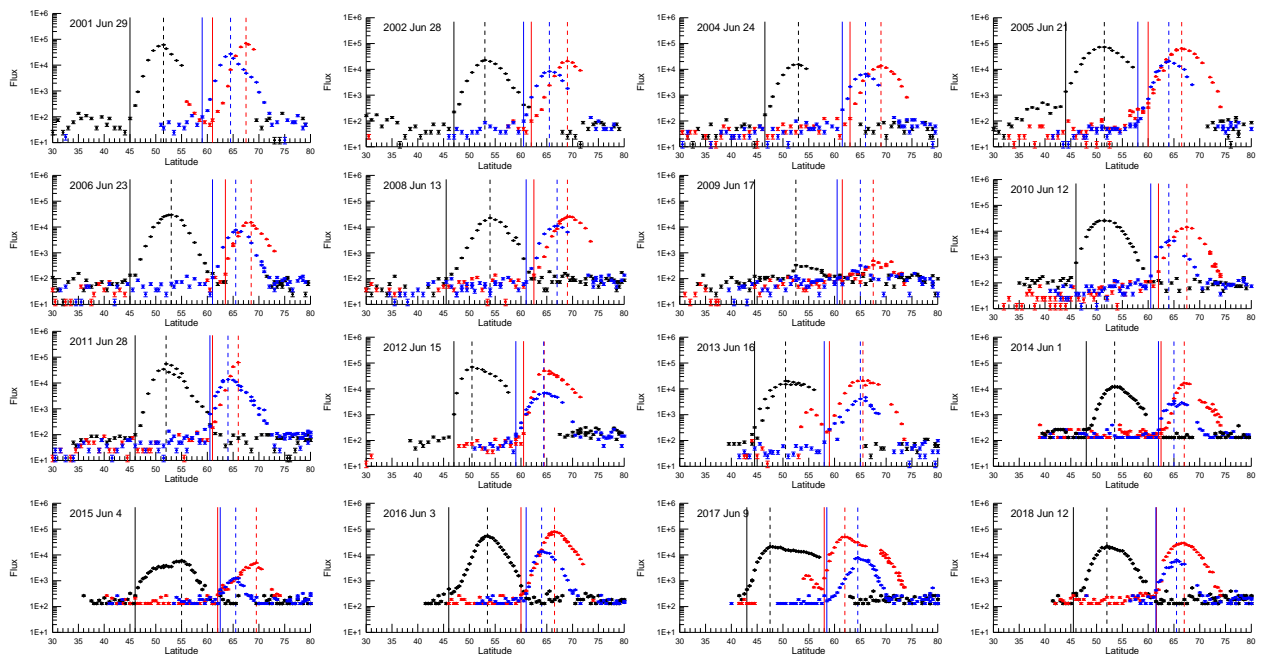


626

627

628

b

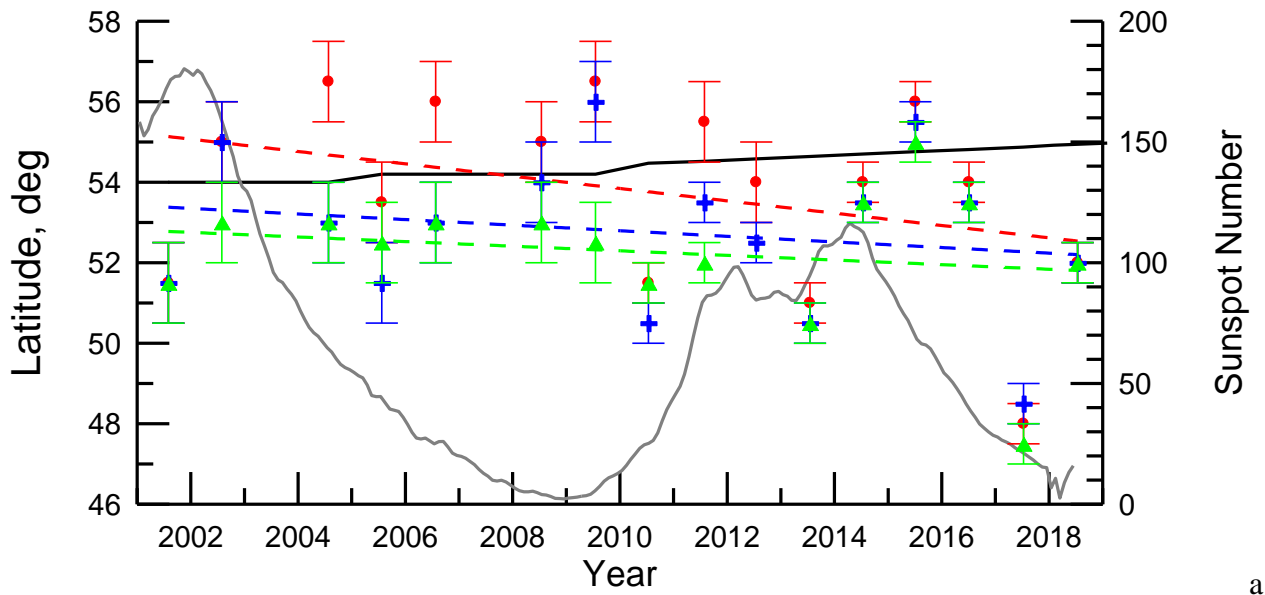


629
 630
 631
 632
 633
 634
 635
 636

Figure 3. Latitudinal profiles of electron fluxes with pitch angles of $\sim 90^\circ$ observed by POES satellites during quiet days in different years at height of ~ 850 km in vicinity of local noon at longitudes around 100°E (red circles), 0°E (blue crosses), and 80°W (black diamonds) for various energy channels: (a) >30 keV, (b) >100 keV, and (c) >300 keV. Vertical dashed and solid lines indicate latitudes of the maximum and inner edge of the outer radiation belt, respectively.

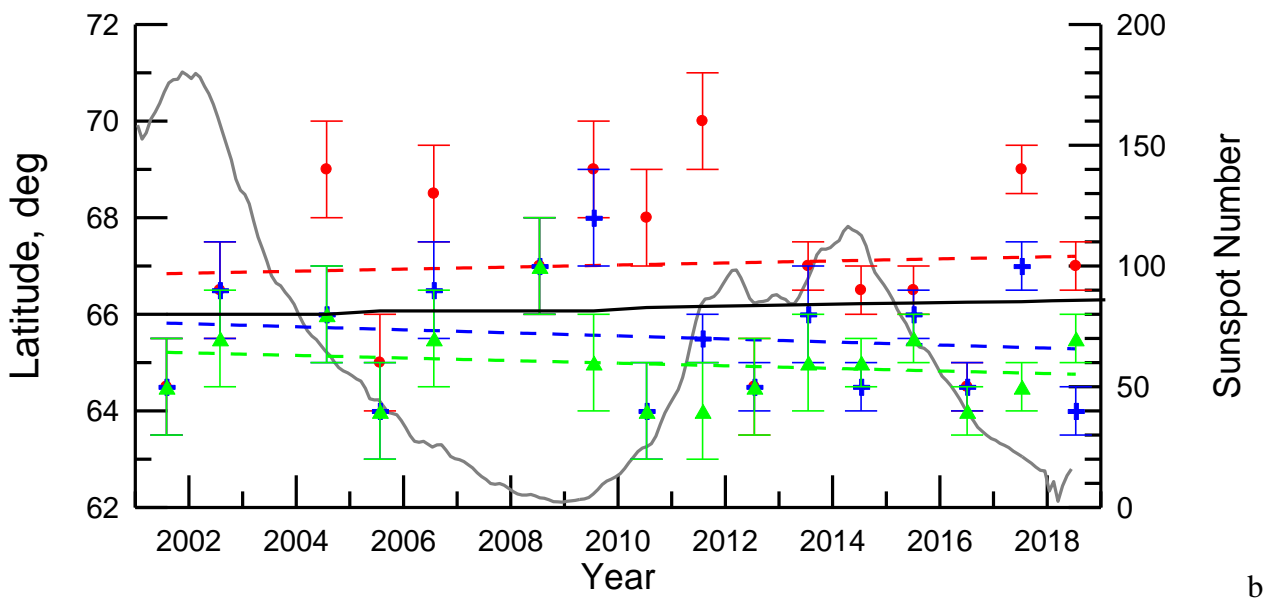
C

637

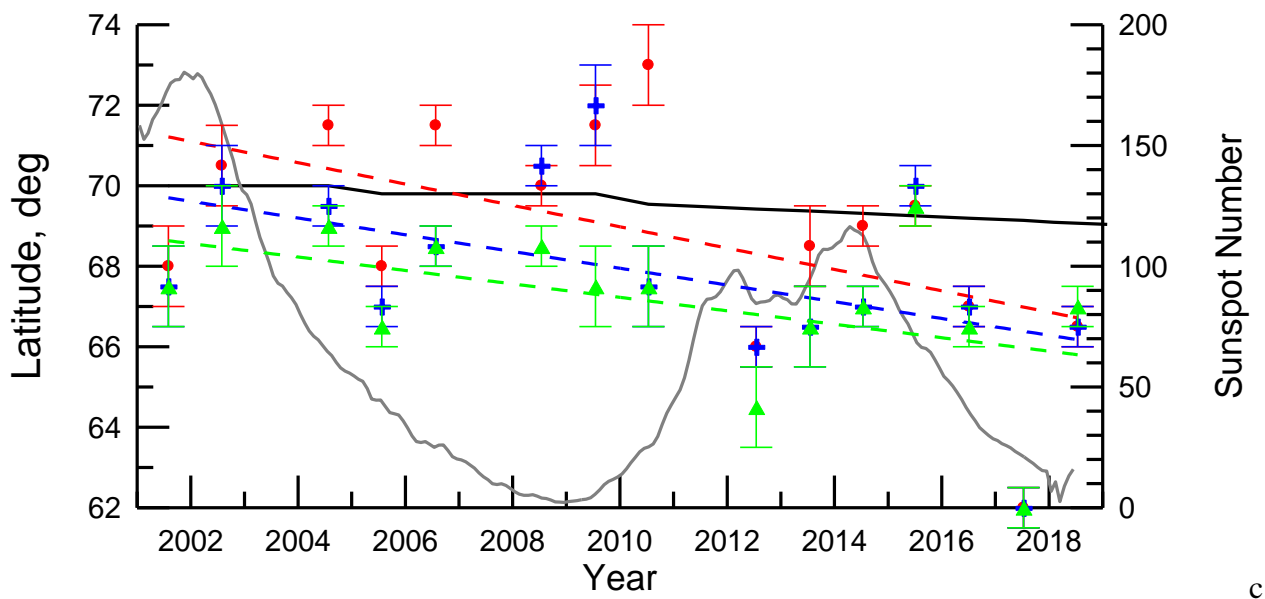


638

639



640



641

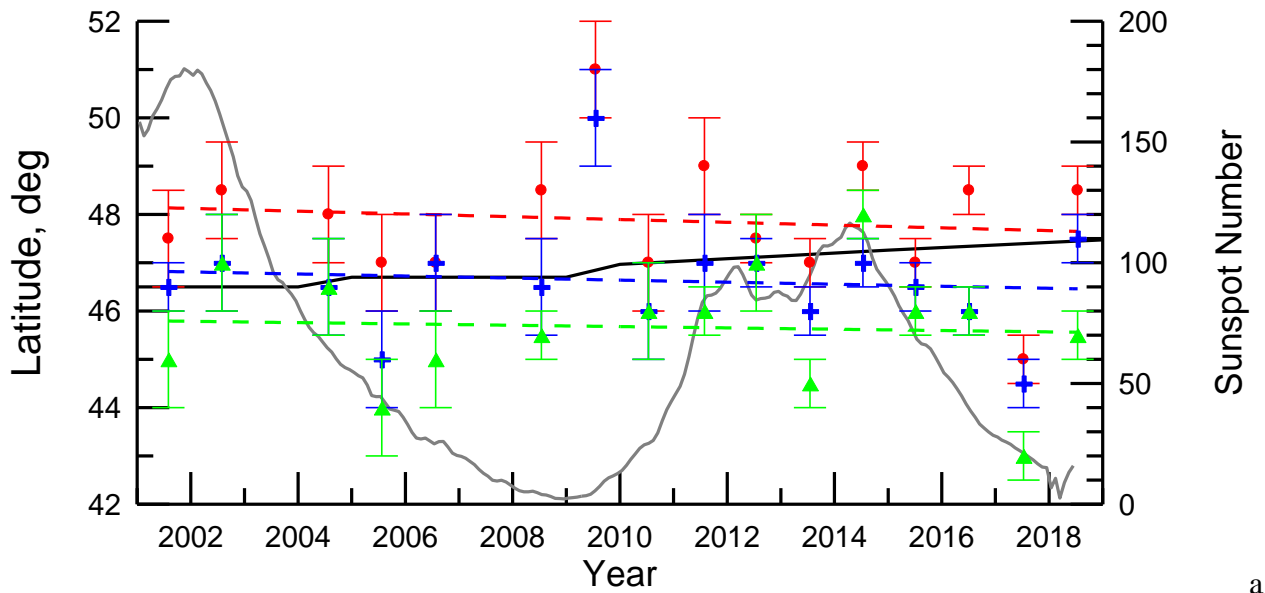
a

b

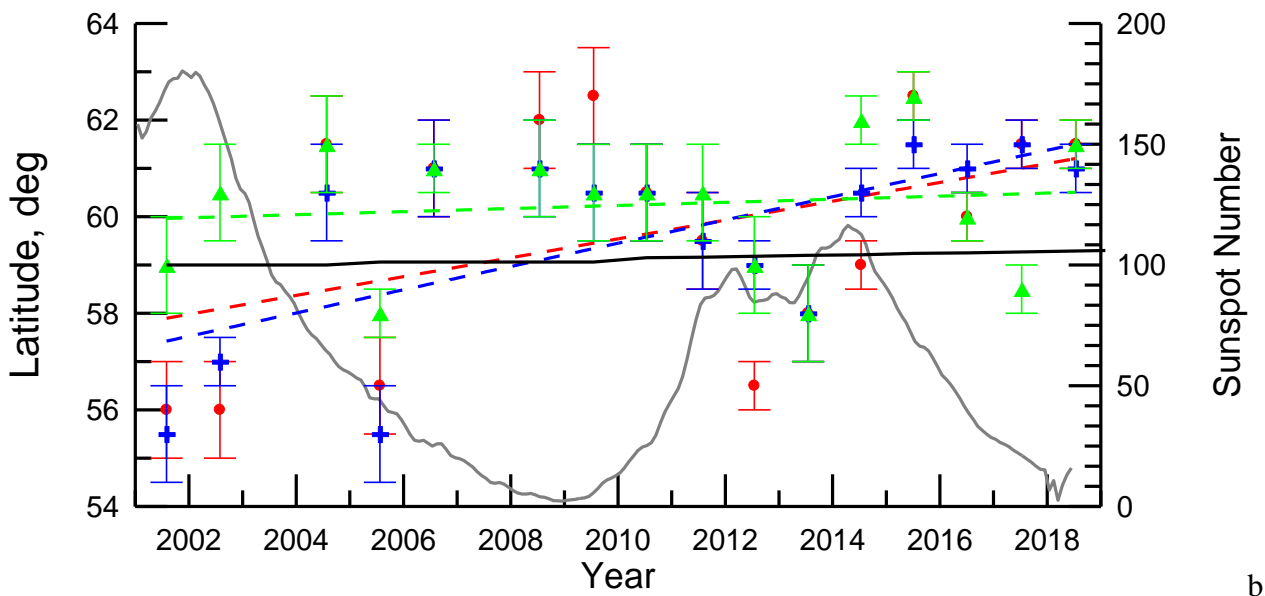
c

642
643 Figure 4. Geographic latitude of the maximum of the outer radiation belt measured at height of
644 ~850 km during geomagnetic quiet days around 80°W (a), 0°E (b), and 100°E (c) for electrons
645 with energies of >30 keV (red circles), >100 keV (blue crosses), and >300 keV (green triangles).
646 Dashed curves of corresponding colors show the best linear fit of the latitudinal change of the
647 maximum location with years (see Table 3). Solid black curves show the latitudinal change
648 predicted by the IGRF model of corresponding epochs (see details in the text). The grey curve
649 shows sunspot number (right axis).
650

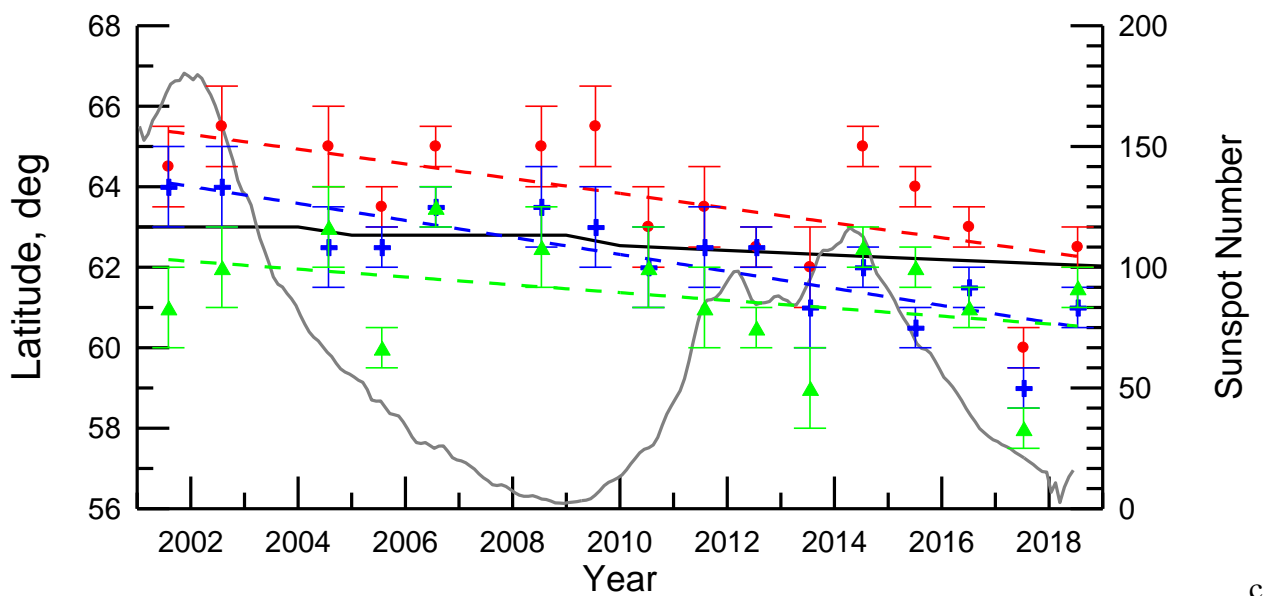
651



652



653

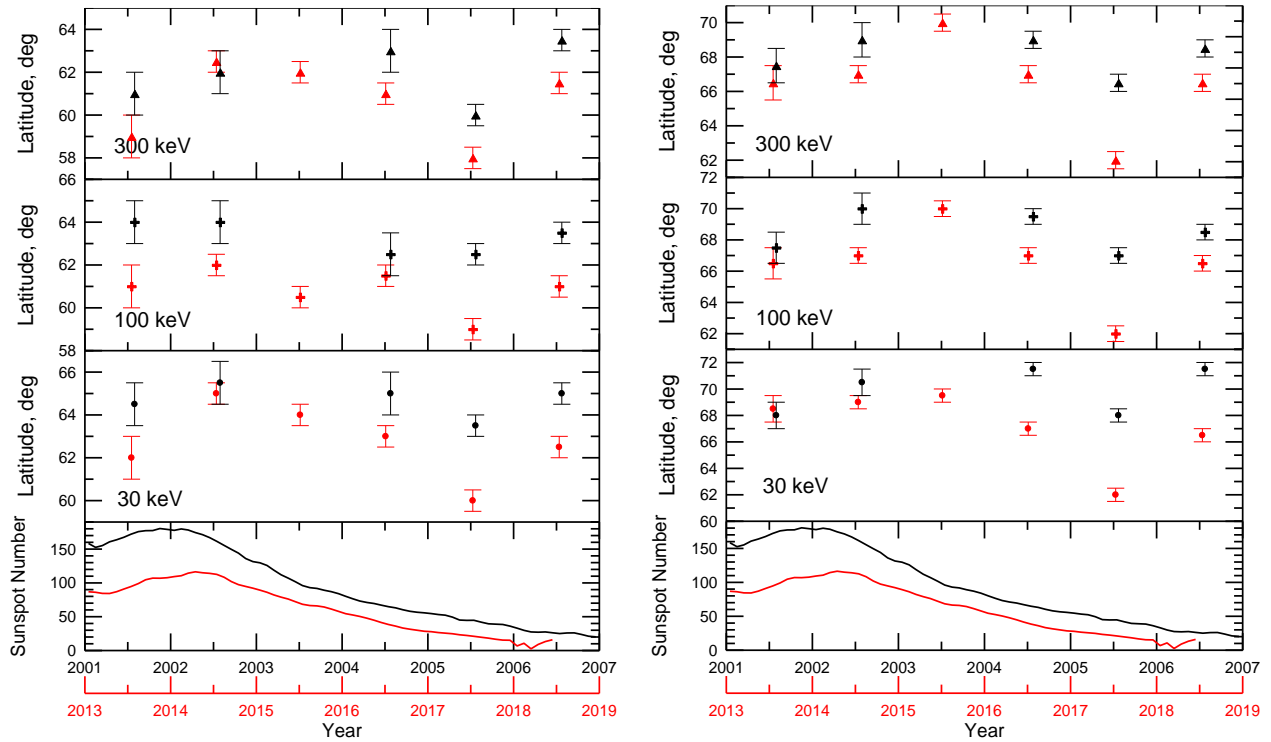


654

655

c

656 Figure 5. The same as Figure 4 but for the inner edge of the outer radiation belt. Coefficients of the
657 best linear fit are presented in Table 4.
658



660

661

662 Figure 6. Geographic latitude of the inner edge (a) and maximum (b) of the outer radiation belt
 663 measured during geomagnetic quiet days at height of ~ 850 km around longitude of 100°E for
 664 electrons with energies of >30 keV (circles), >100 keV (crosses), and >300 keV (triangles).
 665 Bottom panels show the sunspot number in the 23rd solar cycle (the years 2001 – 2006, black
 666 curves) and in the 24th solar cycle (the years 2013 – 2018, blue curves). The outer radiation belt
 667 location is shown by black and red symbols, respectively, for the 23rd and 24th solar cycles. It can
 668 be seen that on the declining phase of the 24th solar cycle, the outer radiation belt is systematically
 669 located at lower latitudes than that during the 23rd solar cycle.

670